Plasticity in crystalline-amorphous core-shell Si nanowires controlled by native interface defects

Julien Guénolé, Julien Godet, Sandrine Brochard

Plasticity in crystalline-amorphous core-shell Si nanowires controlled by native interface defects

Julien Guénolé,* Julien Godet, and Sandrine Brochard

Institut Pprime, UPR 3346, CNRS - Université de Poitiers - ENSMA, SP2MI, B.P. 30179, 86962 Futuroscope Chasseneuil Cedex, France

(Received 4 September 2012; revised manuscript received 30 November 2012; published 2 January 2013)

Experimentally the silicon nanowires or nanopillars are naturally recovered by a thin oxide layer as soon as they are exposed to the air or present an amorphous layer of silicon when they are milled by focused ion beam (FIB) techniques. Here we investigate the role of the silicon amorphous shell on the plasticity of Si nanowires (NWs), thanks to molecular dynamics simulations. It is shown that the yield strain for the nucleation of the first dislocation is decreased for NWs with an amorphous shell when compared to pristine nanowires. For NWs with circular cross-sections, it is shown that the shell thickness has no influence on the yield strain. Besides, through the investigation of various rhombic cross-sections we observe that when an amorphous shell is present, the yield strain is independent of the cross-section shape. All these results can be explained by the presence of native atomic defects at the crystalline/amorphous interface, as revealed by a detailed atomistic analysis. These defects act as seeds for the dislocation nucleation. As a consequence this work raises the question about the role of point defects created in micro- and nanopillars milled by FIB techniques, in particular when they are used to study the mechanical properties at the nanoscale.

DOI: 10.1103/PhysRevB.87.045201 PACS number(s): 62.23.Hj, 62.20.F−

I. INTRODUCTION

Thanks to the development of the experimental techniques to probe the physical properties at the nanoscale, amazing modifications of those properties compared to their bulk counterparts have been revealed. In particular most of the materials exhibit a huge yield stress at nanoscale, close to the theoretical yield stress calculated in single crystal, as for example in metals such as fcc Ni[1] or Cu[2] or bcc Mo,[3] and more surprisingly in brittle semiconductors such as silicon.[4–6] Different mechanisms have been proposed to explain the strengthening in nanostructures,[1,7,8] but most of experimental studies suggest that when the dimensions go down below the micrometer, the usual dislocation bulk sources cannot operate like in bulk materials:[9–12] They are too few and/or hindered. Therefore new sources, such as surface ones, must come into play, and the yield stress must then be very high for activating these new dislocation sources.[3,13–18] The experimental results then confirm the high yield stresses predicted by atomistic simulations performed in defect-free nanostructures like in metals[13] or in silicon.[19] At such high stresses the plasticity may become even more complex with the activation of secondary slip systems like in silicon nanowires.[20]

Interestingly, while most semiconductors are brittle in their bulk form at room temperature, they become ductile below few hundreds of nanometers as recently shown in Si nanowires[21] (NWs), micropillars,[22] and nanospheres[18] or in GaAs[23] and InSb[24] micropillars. This additional size effect is currently referenced as the brittle-ductile transition at low scale. On the other hand, the fact that semiconductor nanostructures can sustain huge elastic strain without crack formation is at the origin of elastic strain engineering.[25] By only varying the strain inside the nanostructures it is possible to tune the physical properties such as the electronic mobility[26] as is done in the strained silicon technology used in microelectronics.

Nowadays the core-shell nanowires are investigated as the nanoscale building block for the next generation of transistors,[27] for field effect transistors,[28] high-efficiency light-emitting diodes,[29] or solar cells,[30,31] the electronic properties being partly controlled by the strain thanks to the growth of various epitaxial shells on the semiconductor NWs.[32] However during their ageing, the strain energy stored in the nanowires can be relaxed through the formation of dislocations or even worse through the formation of cracks that can lead to the failure of nanodevices. It is then important to understand well the mechanisms of plasticity in semiconductor nanostructures when they are submitted to high stresses, in order to prevent their ageing. From a fundamental point of view, such knowledge can also provide insights on the specific mechanical properties observed in these nanostructures, such as the brittle-ductile transition at low scale.

In this study we focus on the understanding of the onset of plasticity in semiconductor nanostructures. In order to access the atomic details of the dislocation nucleation, we used atomistic simulations that are now able to model NWs with relevant sizes similar to those in experiments. We chose silicon as a model for semiconductors and because there is a large variety of well-tested classical potentials able to correctly describe the mechanical properties. Previous numerical studies were performed on the evolution of the yield stress in model silicon NWs with different cross-sections,[33–35] different surface orientations,[36] as a function of the strain rate[35,37] and the size,[38] or by the comparison of the yield stress in full or cagelike NWs,[39] while others investigated the plasticity mechanisms in model Si NWs[36,38] or in polycrystalline NWs.[40] But very few simulations have been done so far to examine the onset of plasticity in core-shell NWs. Such NWs can be deliberately surrounded by a silicon amorphous shell[27,30,41] for technological applications, as mentioned previously. But core-shell NWs are also representative of most realistic NWs that are often naturally covered by a thin amorphous oxide shell as soon as they are exposed to the air.[6,28,42,43] By means of molecular dynamics simulations, Jing *et al.*[44] reported a modification of the Young modulus and the bending and torsion stiffness in crystalline-amorphous Si core-shell NWs, according to the core-shell dimensions, but no significant variation of the yield strain was observed. However, we have

shown previously that the onset of plasticity in semiconductors is very dependent on the surface detailed geometry[36] or on the surface termination like in the case of hydrogen passivated surfaces,[45] so that the presence of an amorphous shell should play a significant role on the onset of plasticity in silicon NWs.

In this paper we present a study of the role of an amorphous shell in the process of dislocation nucleation in silicon NWs. The amorphous silicon shell can be considered as a surrogate of an oxide shell. Indeed, the empirical potentials, necessary to model quite large systems, are not reliable to properly describe the charge transfer at the Si-SiO_2 interface. In particular we have compared model NWs (without amorphous shell) and crystalline-amorphous core-shell NWs, to understand the role of the surface nature on the onset of plasticity. While dislocations are nucleated from the surface defects in pristine SiNWs, we have observed that they are initiated from interface defects in core-shell NWs. This result raises a lot of questions concerning the influence of the focused ion beam technique known to introduce many surface defects[46,47] or even amorphous layers during micropillar milling, in particular when they are used for studying the mechanical properties.

The paper is organized as follows. In Sec. II, we first present the computational methods and the systems used in our work. We then describe the amorphization processes and analyze the obtained amorphous phases. The deformation tests are presented and discussed in Sec. III.

II. METHODOLOGY

A. Computational methods

Due to the large number of atoms in the studied nanostructures (up to 4×10^5) and to avoid thermal uncertainties, classical static simulations are mainly performed for the deformation tests presented in Sec. III. The energy minimization of the systems is performed by the conjugate gradient (CG) algorithm as implanted in the code LAMMPS.[48] The stopping criterion set at 10^{-6} (unitless) is defined as the ratio of the energy variation between two successive iterations, and the energy value. In addition, to reinforce static results, molecular dynamics (MD) simulations are also performed using the Verlet algorithm with an integration time step $\Delta t = 0.5$ fs,[49] and with the temperature controlled by a Nosé-Hoover thermostat[50] in the *NVT* ensemble. The building of the surfaces or shell structures of the studied NWs is made before any deformation test using relaxations both at 0 K and with temperature, as detailed in Secs. II B and II C.

The atomic interactions are described by the well-tested[20,51] Stillinger-Weber (SW) empirical potential based on a combination of two- and three-body terms.[52] Previous studies of the plastic deformation of silicon nanostructures using the SW potential have revealed an unusual behavior with the formation of a characteristic stacking fault under antitwinning shear stress.[33,36] This default has been identified as an artifact of the SW potential.[53] However, this drawback can be avoided by adjusting the three-body part of the potential.[54] We have then set the prefactor of the three-body part λ to 31, which has also the advantage of preventing the large number of overcoordinated atoms in amorphous silicon (a-Si) produced by the standard SW potential,[55] and which improves by the way the quality of the obtained a-Si. We have also set the cohesive energy at the experimental value of 4.63 eV per atom.

B. System geometry

In this work, we choose NWs oriented along the [123] direction that present a single slip mode for the plasticity. Two kinds of section shape are directly cut from bulk silicon, the circular [Fig. 1(a)] and the rhombic [Figs. 1(b) and 1(c)]. SiNWs with circular cross-section shape (c-SiNWs) are close to those commonly studied experimentally[27,56,57] and present no edges which could concentrate the stress.[17,58] SiNWs with a rhombic cross-section shape (r-SiNWs) allow studying the influence of the angle and surface types on the SiNWs' plastic behavior, by adjusting the angle values. As shown in Figs. 1(b) and 1(c), we fix the {111} surfaces and adjust the acute angles (α) in order to build a large variety of rhombic cross-section shapes. Most of the surfaces obtained by this way are of high index, which leads to complex surface structures. A specific rhombic configuration [Fig. 1(b)], called "square" in

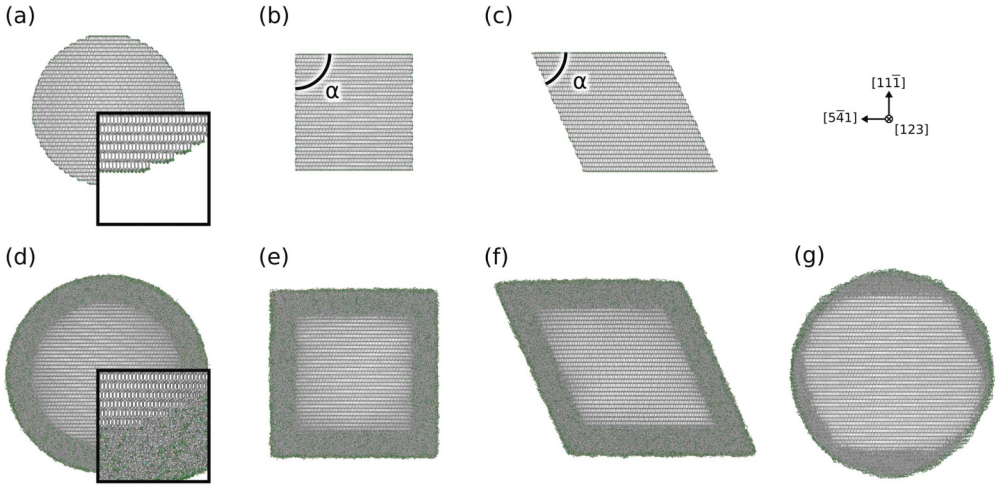

FIG. 1. (Color online) Top view of monocrystalline SiNWs with circular (a) and rhombic cross-section $\alpha = 90^\circ$ (b) and $\alpha = 66^\circ$ (c) and their core-shell counterparts (d), (e), (f) respectively, where the amorphous shell of about 2 nm is produced by the random method. (g) shows a core-shell SiNW produced with the melting method.

the following, is obtained when $\alpha = 90^\circ$ and was previously studied in detail elsewhere.[36]

We can perform precise comparison between such different section shapes, provided that they have the same perimeter.[59] Accordingly, the radial dimensions of the crystalline NW part are set to 12.7 nm and 10.0 nm for the c-SiNW diameter and the r-SiNW side, respectively. The height-over-width ratio for the crystalline parts of c-SiNWs is around 3:1, with the height equal to 38.6 nm to ensure periodic boundaries conditions (PBCs) along the [123] direction. However, with such length, thin r-SiNWs (with small α angle) undergo bending during the compression, which is not in the scope of this study. We then fix the height of r-SiNWs to 18.3 nm, both to prevent bending and ensure PBCs. This choice is supported by some calculations of the critical strain performed for c-SiNWs with several height-over-width ratios fixed in between 0.25 and 3, which show no significant effect on the elasticity limit or on the first plastic events. Therefore, despite the differences between the height-over-width ratios of the c-SiNWs and r-SiNWs above described, we assume that the mechanical responses of these nanostructures can be rigorously compared.

We have considered NWs with and without an amorphous silicon shell. The NWs' surface structures are built by means of different methods. Without the amorphous shell [Figs. 1(a)–1(c)], periodically reconstructed surfaces are obtained using MEAM-Baskes potential[60] while minimizing the system energy. Here the MEAM-Baskes potential is used rather than SW, since it spontaneously yields surface reconstruction at 0 K, while SW does not.[61] We have also investigated surfaces obtained by annealing the NWs at 300 K during 30 ps with SW potential; these kinds of surfaces will be called "annealed" in the following. For core-shell NWs, an amorphous shell has been added on the crystalline NWs [Figs. 1(d)–1(g)]. The formation of the amorphous silicon is described and analyzed in details in Sec. II C.

The compressive deformations are obtained by scaling the simulation cell and the atom positions along the [123] direction (NW axis), with strain increments small enough to ensure good transversal relaxation. For static simulations, strain increments are fixed to -0.1% and followed by an energy minimization as described in Sec. II A. For MD, calculations are performed for 25 ps after each strain increment of -0.5%. The strain rate is then of the order of 10^8 s^{-1}, which, though being huge compared with experimental ones, is typical of MD simulations.[38,58,62] A reduction of the yield strain is expected when reducing the strain rate,[36,58] and a change of the mechanism of plasticity cannot be precluded. However, since the same mechanism of plasticity is observed for all deformation tests presented here, and since this mechanism is obtained at low temperature, it can be safely assumed that there is no effect of the strain rate on the variations of the elasticity limit for a given temperature[58] or on the type of dislocation formed.[36] The conclusions of our work should consequently be the same with different (smaller) strain rates.

C. Amorphous silicon: Construction and analysis

1. Amorphous silicon bulk

(a) Elaboration. In a recent study, Treacy *et al.*[63] evidenced amorphous bulk silicon as a paracrystalline structure. They found that the well known continuous-random-network (CRN) model appears not appropriate to describe a-Si. The reduced density function obtained by electron diffraction and variance data from fluctuation electron microscopy revealed local cubic crystalline silicon clusters embedded in an a-Si phase. Finally, they determined the periodicity of the clusters from 1 to 2 nm.

Our present work aims at studying realistic nanostructures, which are commonly covered by a thin amorphous shell formed during oxidization or chemical vapor deposition, for example. In particular, their thicknesses are of the order of the cluster periodicity observed by Treacy *et al.*, and then are too small to contain a significant number of crystalline clusters. Moreover, as will be described in Sec. III, plastic events are initiated at the core-shell interface so that they should be weakly affected by the clusters inside the amorphous shell. Accordingly, instead of using a paracrystalline model to produce the thin a-Si shell, more classical approaches should be suitable for the study of the very first stages of plasticity in the core-shell SiNWs considered in our work. Two traditional approaches are therefore considered here to build amorphous bulk silicon: the well-used melting-annealing process and a simple random distribution.

The most common method to obtain an amorphous bulk phase is to melt crystalline bulk silicon, and then to quench the system. In the following, we name this amorphous structure "melted." We first set the velocity of all atoms according to the Boltzmann distribution, scaled to produce a temperature of 4500 K.[64] Then, we apply a Nosé-Hoover thermostat in the *NPT* ensemble to maintain the temperature and to stabilize the system for 60 ps, with the external pressure set to zero. Molten bulk silicon is thus obtained. Finally, we quench the system down to about 10 K with a quench rate of 10^{13} K/s and with the external pressure still set to zero. The energy is then minimized, as described in Sec. II A. The main advantage of this approach is that a good amorphous phase quality can be obtained since realistic natural processes of melting are thus modeled. In addition, the amorphous phase quality can be improved by doing several annealing-quenching cycles. Nevertheless, the quality of the amorphous phase is strongly dependent on the quenching rate,[54] resulting in significant cost in CPU time to obtain high-quality amorphous phases.

An alternative method to make amorphous silicon consists in using a random distribution of atoms, followed by an annealing of the system. In the following, we named the amorphous structure thus obtained "random." More precisely, we set a random distribution of atoms in accordance with the silicon crystal density, as implemented in the code LAMMPS.[48] Then, we statically relax the system to prevent overlapped atoms and perform an annealing during 60 ps just below the melting temperature, at 2400 K, and with the external pressure set to zero. Finally, as for the melting method, we quench the system down to about 10 K (quench rate equal to 10^{13} K/s and external pressure set to zero) and then minimize its energy.

(b) Analysis. The characterization of the amorphous structures is mainly performed by using the radial distribution functions (RDFs).[54,55,65,66] We performed the same analysis to characterize the quality of the melted and the random amorphous structures. Figure 2 shows the RDFs of crystalline

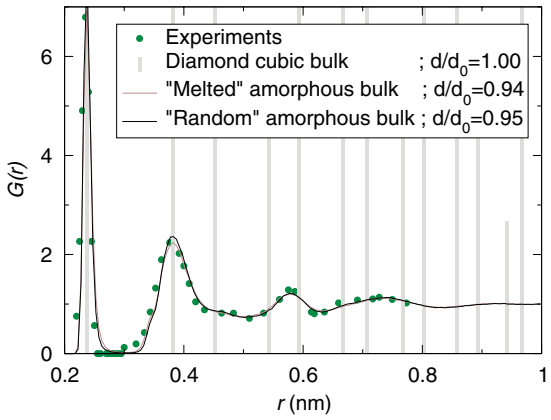

FIG. 2. (Color online) Radial distribution functions (RDFs) of crystalline (gray bars) and amorphous (solid lines) silicon. Green points are experimental data from Laaziri *et al.* (Ref. 65). d/d_0 is the density ratio of the considered structure over that of the diamond cubic structure.

(gray bars) and amorphous bulk silicon (solid lines). As previously reported,[54] we observe a shoulder on the second peak not observed in experiments, characteristic of the SW potential. However, this shoulder is much weaker than the extra peak obtained with original SW potential and it appears nearly merged with the second neighbor's peak. Both numerical methods give RDFs in good agreement with the experimental one,[65] shown with green points in Fig. 2.

We also compare the amorphous formation enthalpy which is 0.33 eV/atom, both for the random and for the melted amorphous structures. Experiments on a-Si produced by ion implantation give an enthalpy of 0.12 eV/atom.[67] Nevertheless, this difference can be explained by considering the different melting points and quench rates between experiments and our simulations. The melting point and the quench rate being much higher than those of experiments, it leads to overestimated enthalpy values in simulations. Finally, the density ratios of the amorphous bulk over that of the crystalline bulk are quite similar for both methods (Fig. 2).

With sufficient relaxation of the initial distribution of atoms during the annealing, we have shown that the random and the melting methods produce equivalent amorphous bulk silicon. In the next section, the building of core-shell structures with both methods is described.

2. *Amorphous silicon shell*

(a) Elaboration. In order to model a core-shell NW, we divide it in two coaxial parts. The inner part is the core and the outer part is the shell, on which the methods described above are applied to obtain the amorphous phase. In the case of core-shell NWs produced by the melting method, the shell part is melted and quenched while the core part is frozen. However, during the quenching of the NWs, recrystallization of the melted part starts from the crystalline/amorphous interfaces (the recrystallization also occurs if the core is not frozen). Except for high quenching rates greater than 10^{14} K/s, melted parts of core-shell NWs appear largely recrystallized after the quenching. Figure 1(g) shows a top view of such a core-shell structure evidencing recrystallization, as compared for example to Fig. 1(d). The irregular interface recrystallization can be limited by a very fast quenching, or a conjugate gradient minimization which can be assimilated to a quenching with an infinite rate. Figure 1(g) also shows surface roughness that appears during the molten process. Since it is intrinsic to the melting method, the occurrence of such roughness cannot be prevented. The amorphous structure therefore looses its cross-section shape.

On the other hand, the random method allows a precise control of cross-section shape and limits recrystallization from interfaces. Indeed, with this method the temperature is chosen below the melting point, so as to restrict both surface roughening and recrystallization from interfaces, while allowing sufficient atoms reorganization to reach a suitable amorphous state. Furthermore, the core part of the NW does not need to be frozen during the whole process. This approach is thus preferred.

Whatever the method used, it is of prime importance to have quantitative elements on the interface position, its thickness, and the quality of the amorphous shell throughout the NW. We have then developed a FORTRAN code which allows a radial scan of the composition of the NW, by means of the RDF function, as detailed in the following.

(b) Analysis. To characterize the NW amorphous shell, we divide the NW into several coaxial tubes of radius R and thickness th, and compare the RDF obtained in each tube to the RDF of a similar tube cut in amorphous bulk silicon. The atoms considered in the tube are those encompassed between a cylinder of radius R and another cylinder of radius $R + th$, and this over the full height of the NW. We first determined the smallest tube thickness allowing the best scan resolution across the NW, that is still enough to describe the amorphous state, and found $th = 0.2$ nm. For a fast and quantitative comparison of RDFs as a function of the tube radius R, we estimate the difference $D(R)$:

$$D(R) = \langle |G^R - G^B| \rangle,$$

where G^R is the RDF of a tube with an inner radius R and a thickness th, virtually cut in the core-shell SiNW; G^B is the RDF of a similar tube, virtually cut in amorphous bulk silicon. $D(R)$ should go to zero when the considered tube is made of a-Si with a structure similar to that of bulk a-Si.

$D(R)$ are shown in Fig. 3 for core-shell NWs with an initial shell thickness of 2.0 nm, obtained with the random method before and after annealing. By definition, $D(R)$ for amorphous silicon is close to zero and in any case lower than $D(R)$ for crystalline silicon. The crystalline-amorphous transition is then clearly evidenced by an abrupt decrease of $D(R)$ in Fig. 3, dividing the curves into two parts between the crystalline core [higher $D(R)$ values] and the amorphous shell [lower $D(R)$ values]. After annealing, the decrease of $D(R)$ is less steep; this suggests a relaxation of the first crystalline layers at the interface leading to a decrease of the interface stresses. In addition, the quality of the amorphous shell after annealing appears in good agreement with the bulk one, as evidenced by the quasinull value of $D(R)$ for $R > 6.6$ nm (Fig. 3). Finally, the extremity of the $D(R)$ curve after annealing increases and shows an extension of the shell radius, which we attribute to the slight surface roughening during the annealing.

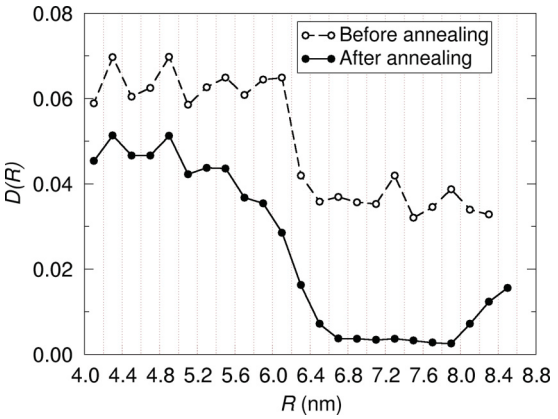

FIG. 3. (Color online) The difference $D(R)$ between the RDF evaluated on a tube extracted from a core-shell NW to this evaluated on a similar tube extracted from amorphous bulk silicon. The amorphous phase is obtained with the random method. The core-shell SiNW has an initial shell thickness of 2.0 nm.

3. Summary

To conclude this part, the random method is more efficient than the melting method to control the thickness of the shell and the position of the core-shell interface along the NW. The subsequent annealing below the melting temperature results in a relatively good quality of the amorphous shell. For this reason we applied this random method to construct the core-shell NWs in most of the simulations described in the following.

III. ONSET OF PLASTICITY IN CRYSTALLINE-AMORPHOUS SILICON CORE-SHELL NWs OF VARIOUS GEOMETRY

The objective of this section is to study the effects of the cross-section shape and the amorphous shell on the very first stages of plasticity. To this aim, we deformed the NWs with the different surface coatings, obtained as described in Secs. II B and II C. All the deformation tests described here were performed at 0 K to avoid the variations of the yield strain ε_y resulting from the temperature. Note however that the same trends are also obtained for MD calculations at 300 K (not presented here). First and foremost, we will study in Sec. III A the influence of the amorphous shell thickness and of the cross-section geometry on the yield strain ε_y, by means of circular and various rhombic NWs. Then, in Sec. III B, the atomic mechanisms at the origin of the formation of the first dislocation in SiNWs with an amorphous shell will be described. Finally, we will discuss these results in Sec. III C. In this work, ε_y is the minimum strain value for which the first plastic event (here the nucleation of the first dislocation) occurs.

A. Geometry and surface/shell effects on the yield strain

1. Role of the amorphous shell thickness: The case of circular NWs

To investigate the role of the amorphous shell thickness, we choose circular NWs with three different surface coatings. Periodically reconstructed surfaces present well-organized structures, such as atomic surface steps,[36] while "annealed" surfaces (Sec. II B) present less organized and nonperiodic

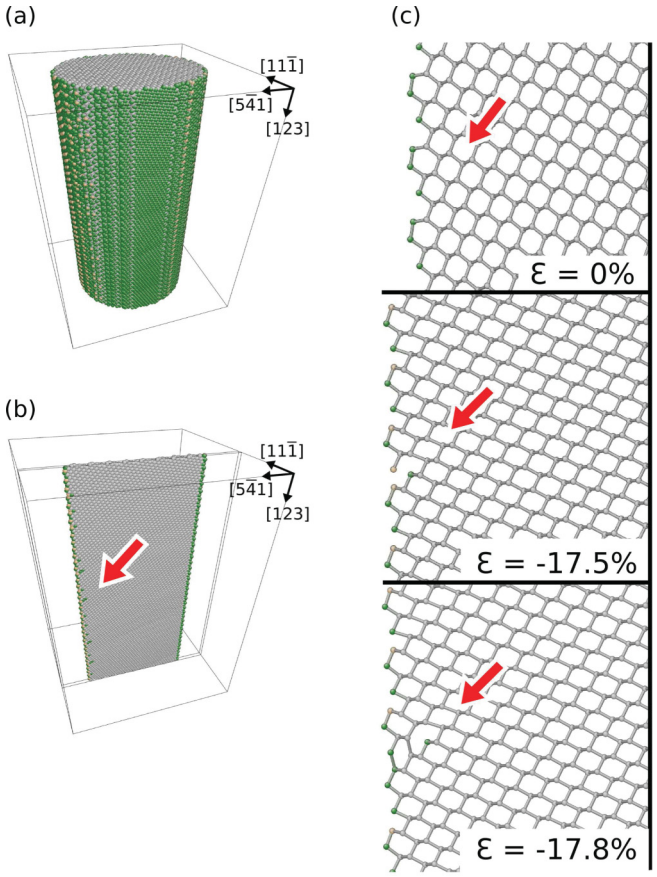

FIG. 4. (Color online) Snapshots of monocrystalline c-SiNW at the yield strain $\varepsilon_y = -17.8\%$ [(a)–(b)]. A slice of two atomic planes is cut from (a) and shown in (b), which encompasses the site of the first plastic event, indicated by a red arrow. The associated mechanism is displayed in (c) for different deformation states (see text for details). The deformation test is performed at 0 K. Atoms are colored according to their coordination number: The brown, green, and gray atoms are respectively 2-, 3-, and 4-fold coordinated.

defects. The deformation tests for NWs with these two kinds of surface states are first considered, and then compared to the case of core-shell NWs with amorphous shells of different thicknesses.

For SiNWs with reconstructed surfaces, surfaces have no singularity and exhibit numerous equivalent defects that are usually organized like surface steps. Figure 4 shows a typical deformation test and the different snapshots of the atomic structure display the mechanism associated to the yield strain at an atomic scale, as described in the following. Figure 4(a) shows the SiNW at the onset of plasticity, with atoms colored according to their coordination number. It may be noted that the surface reconstruction gives most of the time 3-fold coordinated atoms (≈90%) and only few are 2-fold coordinated (≈10%). At the emergence of a characteristic dislocation half loop, a slice of crystal is cut along the NW axis [Fig. 4(b)] to investigate the mechanism presented in detail in Fig. 4(c). The undeformed structure ($\varepsilon = 0\%$) exhibits an atomic surface step at the nucleation site. Not far from the yield strain ($\varepsilon = -17.5\%$), a bond is broken at proximity of the undercoordinated atom at the surface step. At the elasticity limit ($\varepsilon_y = -17.8\%$), a perfect dislocation core is formed and

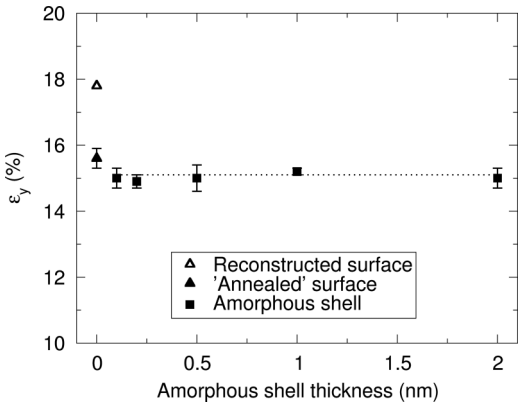

FIG. 5. Compressive yield strain for circular core-shell SiNWs. The empty (full) triangular point corresponds to SiNWs with reconstructed ("annealed") surfaces. The square points are for SiNWs with an amorphous shell and the dotted line is a guide to the eye. The deformation tests are performed at 0 K. For each value, the error bar is determined with two deformation tests carried out on two different NWs, except for the value indicated by the empty triangle for which there is a single surface configuration. In the latter case, the uncertainty can be considered equal to the deformation step, which is 0.1% (not visible in the figure).

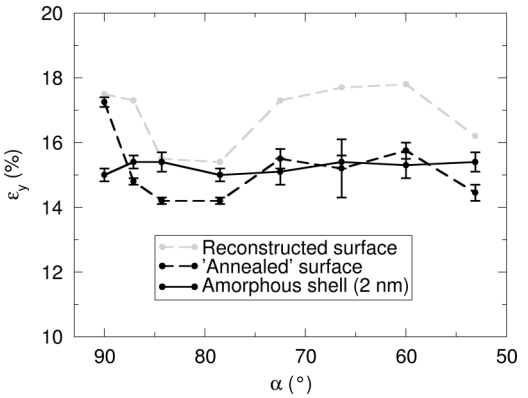

FIG. 6. Compressive yield strain for rhombic core-shell SiNWs versus the acute angle α of the rhombic cross-section. The gray (black) dashed line corresponds to r-siNWs with reconstructed ("annealed") surfaces. The black solid line corresponds to r-SiNWs with an amorphous shell of 2 nm produced by the random method. The lines are only guides for the eye. The deformation tests are performed at 0 K. For each value, the error bar is determined with two deformation tests carried out on two different NWs, except for the NWs with reconstructed surface (see caption of Fig. 5).

slips in a $(\bar{1}11)$ shuffle plane. The mechanism is thus similar to the one observed elsewhere on a model surface step in silicon with classical[19] or *ab initio*[45] calculations.

For NWs with "annealed" surfaces, although the nucleated dislocation remains identical to the one observed with reconstructed surfaces, the yield strain is much lower with a value of −15.6% (Fig. 5, full triangle). So the nonorganized surface defects seems to favor the dislocation nucleation, conversely to the organized ones such as surface steps on NWs with reconstructed surfaces (Fig. 5, empty triangle).

Finally, to investigate the variation of ε_y as a function of the amorphous shell thickness, we produce several c-SiNWs of identical core radius with initial shell thicknesses in between 0.1 and 2.0 nm. Here again, at the yield strain a similar dislocation is nucleated. However, the nucleation occurs at the crystalline-amorphous interface and is described and discussed in detail in Sec. III B. As shown in Fig. 5 (full squares), ε_y remains nearly constant, regardless of the amorphous shell thickness. A similar result has also been obtained previously for smaller c-SiNWs with [111] orientation and another semiempirical potential.[44] Our results confirm that the thickness of an amorphous shell has no influence on the yield strain of SiNWs, at least for the studied dimensions. Furthermore, they show that the yield stress is lower in core-shell systems than in bare NWs with or without periodic surface reconstruction. Since ε_y does not depend on the thickness of the amorphous shell, we use hereafter a shell thickness of 2.0 nm. It can be noted that this thickness is characteristic of the experimental ones for amorphous[41,42] or oxide[27] shells.

2. *Role of the geometry on the yield strain: The case of rhombic NWs, from square to low-angle cross-section*

To investigate the role of the geometry, we now consider rhombic NWs. They can be artificially cut from bulk with any angle, which allows the study of the influence of the opening angle on the plasticity. As the crystallographic orientation of the surfaces or interfaces directly results from the value of the angles, it is possible to obtain r-SiNWs with a large variety of surface types by the mere variation of α. However, such constructions often exhibit high-index surfaces, giving high-energy surfaces. As for the tests on c-SiNWs in the previous section, the analysis is performed on r-SiNWs with three different surface coatings: reconstructed surfaces, annealed surfaces, and finally with an amorphous shell. For r-SiNWs, annealed surfaces are more or less disordered depending on the precise surface crystallography.

For NWs with reconstructed or annealed surfaces, the deformation tests performed on all rhombic NWs show that the nucleation of the first dislocation half loop preferentially occurs from the edges rather than from the flat surfaces (see Table I). Such behavior was previously reported for copper nanowires with square cross-section,[58] and related to the activation volume which is smaller at the corners than at the surfaces. Since our calculations are performed at 0 K, they show that the athermal yield strain, and not only the activation volume, is smaller for dislocation nucleation at the corners than at the surfaces. In any case, we then could expect a role of the opening angle on the onset of plasticity as in metals.[68] However, for NWs with reconstructed surfaces, yield strains ε_y versus the angle α presented in Fig. 6 (gray dashed line) exhibit large variations, without any clear trend according to α. As the NWs are directly cut from bulk silicon according to the chosen angle, the surfaces are high-index ones and exhibit numerous steps. In a previous study,[36] we have shown that the nucleation was strongly correlated to the surface structure. The surface geometry, in particular near the edges, rather than the value of the angles, appears then at the origin of the ε_y variations.

For the case of r-SiNWs with annealed surfaces, the yield strain ε_y versus the angle α is presented in Fig. 6 (black

TABLE I. Occurrence of the nucleation of the first dislocation half loop in rhombic SiNWs with various angle α, as a function of the nucleation site (edge or flat surface). The deformation tests are performed at 0 K, for r-SiNWs with reconstructed or "annealed" surfaces or with an amorphous shell of 2 nm.

	Reconstructed surface		"Annealed" surface		Amorphous shell	
α (degrees)	Edge	Flat surface	Edge	Flat surface	Edge	Flat surface
90	1	0	2	0	1	1
87	1	0	2	0	1	1
84	0	1	2	0	0	2
79	0	1	2	0	0	2
73	1	0	2	0	1	1
66	1	0	1	1	0	2
60	1	0	2	0	1	1
53	1	0	2	0	1	1
Total	6	2	15	1	5	11

dashed line). The variation of ε_y is quite similar to the one above analyzed, despite a global lowering of the critical strain. Moreover, the curve is flatter than in the case of NWs with reconstructed surfaces, suggesting that the impact of the high-index surfaces is softened. However, there is still no clear correlation between the angles and ε_y, so that the surfaces and edges reconstructions, rather than the value of the angles, seem here too at the origin of the yield strain variations.

The case of the square SiNWs ($\alpha = 90^\circ$) is more specific, since we calculate almost the same $\varepsilon_y \approx -17.4\%$ with either the reconstructed or the annealed surfaces (Fig. 6). The square SiNWs present two relatively low index surfaces that are quite stable under temperature annealing. As a result, for square SiNWs the surface state with annealed surfaces is quite similar to the one with reconstructed surfaces, explaining the equivalent yield strains.

Finally, we consider the case of r-SiNWs with amorphous shell (Fig. 6, black solid line). Surprisingly, the variation of ε_y is entirely different from the ones analyzed previously. ε_y remains almost constant, regardless of the value of α. The determining role of the surface structure observed and described above for the r-SiNW with reconstructed and annealed surfaces is completely overridden by the addition of an amorphous shell. The analysis of nucleation sites (Table I) tends to confirm this assertion. While nucleations at edges are privileged in r-SiNWs with the surface reconstructions, nucleations occur either from edges or (preferentially) from flat surfaces in r-SiNWs with an amorphous shell. The interface orientation and the angle value seem to have no influence on the yield strain in core-shell r-SiNWs.

B. Mechanism of dislocations nucleation in core-shell systems

To analyze the plastic mechanisms in core-shell SiNWs, we choose a c-SiNW with an initial shell thickness of 2.0 nm. Nevertheless, analogous results have been observed in c-SiNWs with thinner amorphous shell and in r-SiNWs regardless of α, at 0 K as well as with temperature. Figure 7(a) shows the core-shell c-SiNW for a deformation of $\varepsilon = -15.3\%$, before the yield strain ($\varepsilon_y = -15.5\%$). A slice of two atomic planes is cut along the NW axis; this slice encompasses the site of the first dislocation nucleation, indicated by the red arrow [Fig. 7(b)]. The atomic mechanism is shown in detail in Fig. 7(c). Prior to the deformation ($\varepsilon = 0\%$), the interface presents plenty of structural defects. At first glance, many defects could favor the nucleation. A meticulous analysis of the numerous deformation tests performed using c-SiNWs and r-SiNWs evidences a characteristic point defect. As highlighted in light red in Fig. 7(c), the interface exhibits a local atomic structure close (but not identical) to the structure of a perfect dislocation core. In the following, this structure will be called "corelike." In a perfect diamond cubic structure, the hexagons viewed in {110} planes are made up of 6 atoms 4-fold coordinated, whereas a 60° perfect dislocation has a core formed by 7 atoms 4-fold coordinated and one 3-fold coordinated. Such a core can be seen for example in Fig. 7(c) at −15.3%. As for it, the corelike structure is composed of 7 or 9 atoms mainly 4-fold coordinated. One or two atoms may be 3-fold coordinated, but it is not always the case. In the characteristic case presented in Fig. 7(c) ($\varepsilon = 0\%$), the corelike structure is formed by 7 atoms 4-fold coordinated. During the deformation, this corelike structure undergoes various reconstructions, as for example at the strain level $\varepsilon = -15.3\%$ [Fig. 7(c)] with the appearance of a 3-fold coordinated atom. A classical dislocation core is thus formed. Surprisingly, the core does not slip just after this formation, appearing to be trapped by the interface. The system has to be a little more strained to initiate the slip of the dislocation core, and then reach the elasticity limit [$\varepsilon_y = -15.5\%$; Fig. 7(c)]. Sometimes, the strain difference between the strain level at the formation of a real dislocation core and the yield strain is greater (up to a few percent). Nevertheless, the chain of the modifications from the corelike to the classical dislocation core is quite similar.

It thus appears that the very first plastic event takes its origin at a point defect at the crystalline-amorphous interface. However, all such corelike defects at the interface do not engender the first dislocation. This obvious assertion raises the question of the driving force behind the nucleation. To gain insight into it, we use the local von Mises shear strain invariant,[69] as implemented in ATOMEYE,[70] which allows a good estimation of the shear strain at the atomic level. Figure 7(d) displays the same slice as that described in Figs. 7(b) and 7(c), but colored according to the von Mises shear strain invariant. The core observed in Fig. 7(c) just before

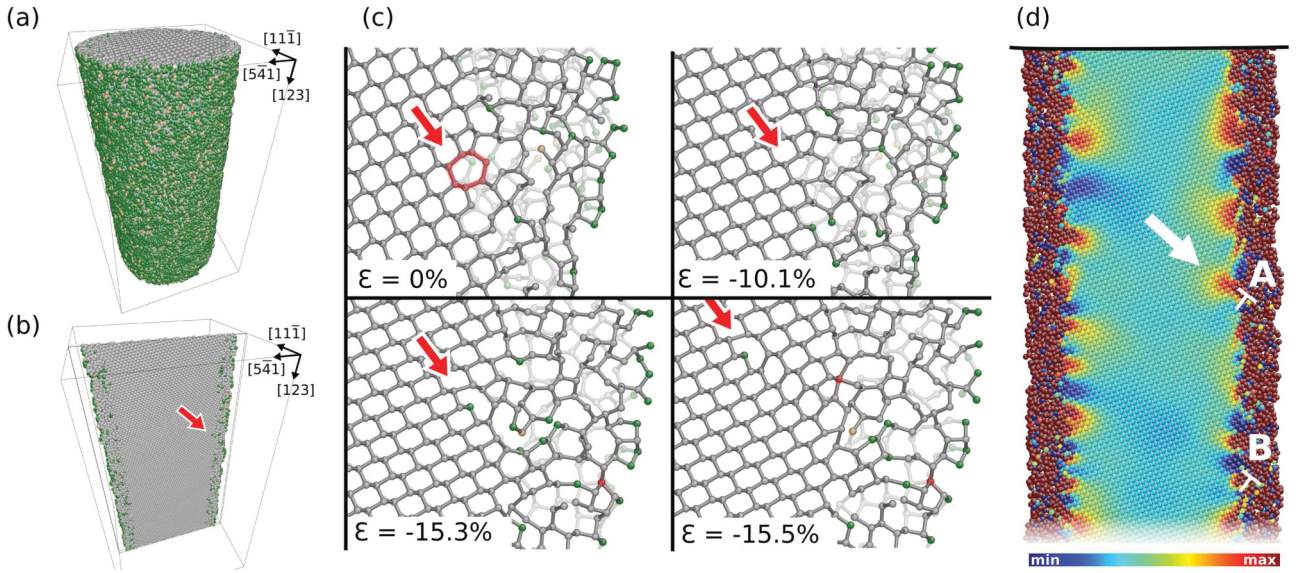

FIG. 7. (Color online) Snapshot of core-shell c-SiNW before the yield strain $\varepsilon_y = -15.5\%$ [(a), (b)]. A slice of two atomic planes is cut from (a) and shown in (b), which encompasses the site of the first dislocation nucleation, indicated by a red arrow. The associated atomic mechanism is displayed in (c) for different deformation states. Atoms are colored according to their coordination number. Snapshot (d) is the same slice as in (b) with atoms colored according to the local von Mises shear strain invariant. The deformation test is performed at 0 K.

the nucleation is called "A" in Fig. 7(d). The core "B" is another corelike point defect located at the crystalline-amorphous interface. The white arrow indicates strain concentration, aligned along the slip direction, close to the core A. No such strain concentration can be observed in the neighboring area of the core B. It seems thus that the core that slips at the yield strain is determined by this local strain concentration before yield. Despite the difficulties to determine precisely the origin of such concentration, we can reasonably assume a decisive role of the interface roughness resulting from the annealing realized during the amorphous shell formation, before the deformation tests.

C. Discussion

In Sec. III A, it has been shown that the presence of amorphous shells strongly influences the yield strain of SiNWs. By the addition of an amorphous shell, ε_y is lowered compared to bare NWs. The theory of elasticity can be invoked to explain this lowering; indeed, the image force is expected to be reduced when a free surface is replaced by a crystalline-amorphous interface. Since the image force attracts the dislocation towards the surface (or towards the crystalline-amorphous interface), its reduction is consistent with a lowering of ε_y. However, this is a coarse analysis assuming planar interfaces separating semi-infinite media, and the accurate determination of the image force in the case of core-shell nanowires is quite difficult to perform, even in the framework of linear isotropic elasticity. Furthermore, if an image effect would be important for the systems considered in this study, it would entail an influence of the shell thickness on the yield strain, which is not observed here. The mechanism of dislocation nucleation described in Sec. III B rather suggests that the lowering of the yield strain is due to the presence of corelike defects at the crystalline-amorphous interface. Such defects act as new seeds for dislocation nucleation. Since they are interface defects, the shell thickness has no influence on their activation, and consequently on the yield strain.

Besides, while the surface and edge structures seem to be the key parameters for the control of the onset of plasticity and the associated yield strain for SiNWs with perfectly reconstructed surfaces, this effect disappears as soon as the surface loses its periodic arrangement and in particular, in the presence of a thin amorphous layer. In the latter case, the yield strain remains approximately constant whatever the interface orientation is (Fig. 6). In addition, for the rhombic NWs, the edges stop to be a favored site for the beginning of plasticity when a thin amorphous shell is present. The cross-section shape of the NW seems to have no effect on the onset of plasticity once it is covered by a thin amorphous layer. This is confirmed by comparing the yield strain for the circular core-shell SiNWs (Fig. 5) to that obtained for the rhombic core-shell SiNWs (Fig. 6): They are equivalent. Conversely, without the amorphous shell, the yield strain obtained for the circular SiNWs is slightly different from that obtained for the square SiNWs, in agreement with the results observed by Yang *et al.*[33] Once again, the role of the corelike defects is essential: Since they are native point defects, their activation and consequently the yield strain are not dependent on the specific cross-section shape. As experimentally the SiNWs are always covered by an amorphous layer, most of the time an oxide, we can expect that the plasticity of real semiconductor NWs does not depend on their cross-section geometry, but should only depend on the stress orientation through their growth axis.

Note that the corelike defects are *a priori* not present at (semi)coherent interfaces, so that the results emphasized here are not relevant for core-shell NWs with such interfaces, in which misfit dislocations can come into play.[71,72] The corelike defects must be particularly important for

amorphous-crystalline interfaces of covalent materials in general; indeed the directionality of the atomic bond in these materials makes prominent the effects related to dislocation cores.

Finally, we want to mention that at present there is no experimental study that directly shows the role of only the cross-section geometry or the amorphous layer thickness on the elasticity limit. For SiNWs with similar cross-section sizes under tensile loading, Kizuka *et al.*[4] on the one hand and Zhu *et al.*[21] on the other hand have reported comparable elasticity limit/fracture strain for NWs with seemingly different cross-section shapes and amorphous layers. But these experimental works were carried out with NWs of different axis, and besides they did not yield the same mechanism of plasticity. In this context, our results must therefore be considered as predictive.

IV. CONCLUSION

We have performed classical atomistic simulations to investigate the onset of plasticity in core-shell crystalline-amorphous SiNWs under uniaxial compressive strain. Using a modified Stillinger-Weber potential and specific amorphization processes, we have produced high-quality amorphous shells with well-controlled shapes. Careful atomic structure analyses have allowed us to evidence the crucial role of the amorphous shell on the very first stages of plasticity. In pristine NWs, we have observed dislocation nucleation from surfaces, as previously reported.[17,36,45] In core-shell NWs, the crystalline-amorphous interface is deciding for the onset of plasticity: It modifies both the elasticity limit and the dislocation nucleation sites. Indeed, we have observed that intrinsic point defects at the interface, similar to a 60° dislocation core structure, evolve during the deformation up to form a real dislocation core, which eventually slips and initiates then plasticity. These native defects then behave like seeds for dislocation nucleation. The evolution of the yield strain is accordingly as follows: For a given NW axis and uniaxial deformation mode, strong variations of the yield strain are observed when changing the surfaces structure of pristine NWs, whereas core-shell NWs have identical yield strain regardless of the interface's orientation or the amorphous shell thickness. The role of the corelike defects in the nonvariation of the yield strain for core-shell NWs is crucial: Since they are native interface point defects, neither the specific cross-section shape nor the shell thickness influences the yield strain. These results obtained for silicon should be particularly relevant for other covalent materials, as far as dislocation nucleation is concerned (which must be most often the case for the smaller NWs).

Experimentally semiconductor nanowires or pillars are in most cases surrounded by a disorganized shell (amorphous or with many surface defects as introduced by focused ion beam techniques, for example). It can then be assumed that for a given NW axis, their plasticity is independent of the cross-section geometry when submitted to uniaxial deformation. To go further, the results evidenced in this paper can serve as a support to study the ability of tuning some mechanical properties of initially pristine nanostructures by simply controlling the surrounding shell.

*julien.guenole@univ-poitiers.fr

[1] M. D. Uchic, D. M. Dimiduk, J. N. Florando, and W. D. Nix, Science **306**, 1134 (2004).

[2] D. Kiener, C. Motz, T. Schoeberl, M. Jenko, and G. Dehm, Adv. Eng. Mat. **8**, 1119 (2006).

[3] H. Bei, S. Shim, G. Pharr, and E. George, Acta Mat. **56**, 4762 (2008).

[4] T. Kizuka, Y. Takatani, K. Asaka, and R. Yoshizaki, Phys. Rev. B **72**, 035333 (2005).

[5] S. Hoffmann, I. Utke, B. Moser, J. Michler, S. H. Christiansen, V. Schmidt, S. Senz, P. Werner, U. Gösele, and C. Ballif, Nano Lett. **6**, 622 (2006).

[6] X. D. Han, K. Zheng, Y. F. Zhang, X. N. Zhang, Z. Zhang, and Z. L. Wang, Adv. Mater. **19**, 2112 (2007).

[7] J. R. Greer and W. D. Nix, Phys. Rev. B **73**, 245410 (2006).

[8] S. H. Oh, M. Legros, D. Kiener, and G. Dehm, Nat. Mater. **8**, 95 (2009).

[9] Z. W. Shan, R. K. Mishra, S. A. S. Asif, O. L. Warren, and A. M. Minor, Nat. Mater. **7**, 115 (2008).

[10] S.-W. Lee, S. M. Han, and W. D. Nix, Acta Mat. **57**, 4404 (2009).

[11] D. Kiener and A. M. Minor, Nano Lett. **11**, 3816 (2011).

[12] C. Chisholm, H. Bei, M. Lowry, J. Oh, S. S. Asif, O. Warren, Z. Shan, E. George, and A. Minor, Acta Mat. **60**, 2258 (2012).

[13] S. Brochard, P. Beauchamp, and J. Grilhé, Philos. Mag. A **80**, 503 (2000).

[14] S. Oh, M. Legros, D. Kiener, P. Gruber, and G. Dehm, Acta Mat. **55**, 5558 (2007).

[15] D. Kiener, W. Grosinger, G. Dehm, and R. Pippan, Acta Mat. **56**, 580 (2008).

[16] J. Godet, P. Hirel, S. Brochard, and L. Pizzagalli, J. Appl. Phys. **105**, 026104 (2009).

[17] S. Izumi and S. Yip, J. Appl. Phys. **104**, 033513 (2008).

[18] J. Nowak, A. Beaber, O. Ugurlu, S. Girshick, and W. Gerberich, Scr. Mater. **62**, 819 (2010).

[19] J. Godet, L. Pizzagalli, S. Brochard, and P. Beauchamp, Phys. Rev. B **70**, 054109 (2004).

[20] J. Guénolé, S. Brochard, and J. Godet, Acta Mat. **59**, 7464 (2011).

[21] Y. Zhu, F. Xu, Q. Qin, W. Y. Fung, and W. Lu, Nano Lett. **9**, 3934 (2009).

[22] F. Östlund, K. Rzepiejewska-Malyska, K. Leifer, L. M. Hale, Y. Tang, R. Ballarini, W. W. Gerberich, and J. Michler, Adv. Funct. Mater. **19**, 2439 (2009).

[23] F. Östlund, P. R. Howie, R. Ghisleni, S. Korte, K. Leifer, W. J. Clegg, and J. Michler, Philos. Mag. **91**, 1190 (2011).

[24] L. Thilly, R. Ghisleni, C. Swistak, and J. Michler, Philos. Mag. **92**, 3315 (2012).

[25] T. Zhu and J. Li, Prog. Mater. Sci. **55**, 710 (2010).

[26] Z. Cheng, M. Currie, C. Leitz, G. Taraschi, E. Fitzgerald, J. Hoyt, and D. Antoniadas, IEEE Electron Device Lett. **22**, 321 (2001).

[27] L. J. Lauhon, M. S. Gudiksen, D. Wang, and C. M. Lieber, Nature (London) **420**, 57 (2002).

[28] Y. Cui, Z. Zhong, D. Wang, W. U. Wang, and C. M. Lieber, Nano Lett. **3**, 149 (2003).

[29]F. Qian, S. Gradecak, Y. Li, C.-Y. Wen, and C. M. Lieber, Nano Lett. **5**, 2287 (2005).
[30]L. Tsakalakos, J. Balch, J. Fronheiser, B. A. Korevaar, O. Sulima, and J. Rand, Appl. Phys. Lett. **91**, 233117 (2007).
[31]M. D. Kelzenberg, D. B. Turner-Evans, B. M. Kayes, M. A. Filler, M. C. Putnam, N. S. Lewis, and H. A. Atwater, Nano Lett. **8**, 710 (2008).
[32]I. A. Goldthorpe, A. F. Marshall, and P. C. McIntyre, Nano Lett. **9**, 3715 (2009).
[33]Z. Yang, Z. Lu, and Y.-P. Zhao, J. Appl. Phys. **106**, 023537 (2009).
[34]Y. Jing, Q. Meng, and W. Zhao, Physica E **41**, 685 (2009).
[35]Y. Jing, Q. Meng, and Y. Gao, Comput. Mater. Sci. **45**, 321 (2009).
[36]J. Guénolé, J. Godet, and S. Brochard, Model. Simul. Mater. Sci. Eng. **19**, 074003 (2011).
[37]C. Y. Tang, L. Zhang, and K. Mylvaganam, Comput. Mater. Sci. **51**, 117 (2012).
[38]K. Kang and W. Cai, Int. J. Plasticity **26**, 1387 (2010).
[39]M. Menon, D. Srivastava, I. Ponomareva, and L. A. Chernozatonskii, Phys. Rev. B **70**, 125313 (2004).
[40]F. Cleri, T. Ishida, D. Collard, and H. Fujita, Appl. Phys. Lett. **97**, 153106 (2010).
[41]Y. Dong, G. Yu, M. C. McAlpine, W. Lu, and C. M. Lieber, Nano Lett. **8**, 386 (2008).
[42]Y. Cui, L. J. Lauhon, M. S. Gudiksen, J. Wang, and C. M. Lieber, Appl. Phys. Lett. **78**, 2214 (2001).
[43]K. Zheng, X. Han, L. Wang, Y. Zhang, Y. Yue, Y. Qin, X. Zhang, and Z. Zhang, Nano Lett. **9**, 2471 (2009).
[44]Y. Jing and Q. Meng, Physica B **405**, 2413 (2010).
[45]J. Godet, S. Brochard, L. Pizzagalli, P. Beauchamp, and J. M. Soler, Phys. Rev. B **73**, 092105 (2006).
[46]R. Maaß, D. Grolimund, S. V. Petegem, M. Willimann, M. Jensen, H. V. Swygenhoven, T. Lehnert, M. A. M. Gijs, C. A. Volkert, E. T. Lilleodden, and R. Schwaiger, Appl. Phys. Lett. **89**, 151905 (2006).
[47]D. Kiener, C. Motz, M. Rester, M. Jenko, and G. Dehm, Mater. Sci. Eng. A **459**, 262 (2007).
[48]S. Plimpton, J. Comput. Phys. **117**, 1 (1995).
[49]L. Verlet, Phys. Rev. **159**, 98 (1967).
[50]W. G. Hoover, Phys. Rev. A **31**, 1695 (1985).
[51]J. Godet, L. Pizzagalli, S. Brochard, and P. Beauchamp, J. Phys.: Condens. Matter **15**, 6943 (2003).
[52]F. H. Stillinger and T. A. Weber, Phys. Rev. B **31**, 5262 (1985).
[53]J. Godet, L. Pizzagalli, S. Brochard, and P. Beauchamp, Comput. Mater. Sci. **30**, 16 (2004).
[54]C. Fusco, T. Albaret, and A. Tanguy, Phys. Rev. E **82**, 066116 (2010).
[55]R. Vink, G. Barkema, W. van der Weg, and N. Mousseau, J. Non-Cryst. Solids **282**, 248 (2001).
[56]J. Liu, Y. Lu, Y. Shi, S. Gu, R. Jiang, F. Wang, and Y. Zheng, Appl. Phys. A **66**, 539 (1998).
[57]D. D. D. Ma, C. S. Lee, F. C. K. Au, S. Y. Tong, and S. T. Lee, Science **299**, 1874 (2003).
[58]T. Zhu, J. Li, A. Samanta, A. Leach, and K. Gall, Phys. Rev. Lett. **100**, 025502 (2008).
[59]J. F. Justo, R. D. Menezes, and L. V. C. Assali, Phys. Rev. B **75**, 045303 (2007).
[60]M. I. Baskes, Phys. Rev. B **46**, 2727 (1992).
[61]H. Balamane, T. Halicioglu, and W. A. Tiller, Phys. Rev. B **46**, 2250 (1992).
[62]H. Ikeda, Y. Qi, T. Çagin, K. Samwer, W. L. Johnson, and W. A. Goddard, Phys. Rev. Lett. **82**, 2900 (1999).
[63]M. M. J. Treacy and K. B. Borisenko, Science **335**, 950 (2012).
[64]The molten temperature of silicon is on the order of 1600 K with the standard SW potential. With the modifications made in this work on the SW potential ($\lambda = 31$, $E_c = 4.63$ eV/atom), the molten temperature of silicon is of the order of 3000 K.
[65]K. Laaziri, S. Kycia, S. Roorda, M. Chicoine, J. L. Robertson, J. Wang, and S. C. Moss, Phys. Rev. Lett. **82**, 3460 (1999).
[66]M. J. Demkowicz and A. S. Argon, Phys. Rev. B **72**, 245205 (2005).
[67]S. Roorda, S. Doorn, W. C. Sinke, P. M. L. O. Scholte, and E. van Loenen, Phys. Rev. Lett. **62**, 1880 (1989).
[68]C. R. Weinberger, A. T. Jennings, K. Kang, and J. R. Greer, J. Mech. Phys. Solids **60**, 84 (2012).
[69]F. Shimizu, S. Ogata, and J. Li, Mater. Trans. **48**, 2923 (2007).
[70]J. Li, Model. Simul. Mater. Sci. Eng. **11**, 173 (2003).
[71]K. E. Aifantis, A. L. Kolesnikova, and A. E. Romanov, Philos. Mag. **87**, 4731 (2007).
[72]K. L. Kavanagh, Semicond. Sci. Technol. **25**, 024006 (2010).